

# Alkyl-Substituted Selenium-Bridged V-Shaped Organic Semiconductors Exhibiting High Hole Mobility and Unusual Aggregation Behavior

Toshihiro Okamoto,\* Masato Mitani, Craig P. Yu, Chikahiko Mitsui, Masakazu Yamagishi, Hiroyuki Ishii, Go Watanabe, Shohei Kumagai, Daisuke Hashizume, Shota Tanaka, Masafumi Yano, Tomokatsu Kushida, Hiroyasu Sato, Kunihisa Sugimoto, Takashi Kato, and Jun Takeya



Cite This: <https://dx.doi.org/10.1021/jacs.0c05522>



Read Online

ACCESS |



Metrics & More

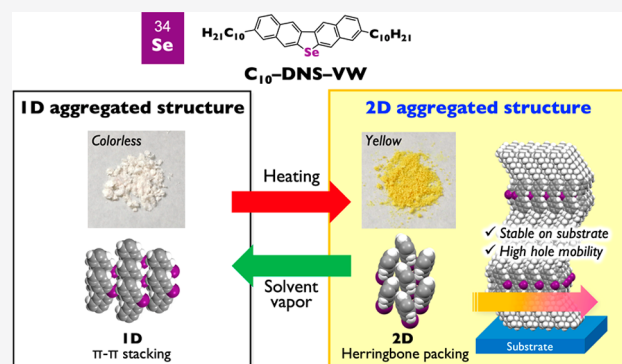


Article Recommendations



Supporting Information

**ABSTRACT:** Toward the development of high-performance organic semiconductors (OSCs), carrier mobility is the most important requirement for next-generation OSC-based electronics. The strategy is that OSCs consisting of a highly extended  $\pi$ -electron core exhibit two-dimensional (2D) aggregated structures to offer effective charge transport. However, such OSCs, in general, show poor solubility in common organic solvents, resulting in limited solution processability. This is a critical trade-off between the development of OSCs with simultaneous high carrier mobility and suitable solubility. To address this issue, herein, five-membered ring-fused selenium-bridged V-shaped binaphthalene with decyl substituents ( $C_{10}$ -DNS-VW) is developed and synthesized by an efficient method.  $C_{10}$ -DNS-VW exhibits significantly high solubility for solution processes. Notably,  $C_{10}$ -DNS-VW forms a one-dimensional  $\pi$ -stacked packing motif (1D motif) and a 2D herringbone (HB) packing motif (2D motif), depending on the crystal growth condition. On the other hand, the fabrication of thin films by means of both solution process and vacuum deposition techniques forms only the 2D HB motif. External stress tests such as heating and exposure to solvent vapor indicated that 1D and 2D motifs could be synergistically induced by the total balance of intermolecular interactions. Finally, the single-crystalline films of  $C_{10}$ -DNS-VW by solution process exhibit carrier mobility up to  $11 \text{ cm}^2 \text{ V}^{-1} \text{ s}^{-1}$  with suitable transistor stability under ambient conditions for more than two months, indicating that  $C_{10}$ -DNS-VW is one of the most promising candidates for breaking the trade-off in the field of solution-processed technologies.



## 1. INTRODUCTION

In the area of printed and flexible electronics with organic semiconductors (OSCs), control of molecular ordering and resultant molecular orbital overlaps of OSC molecules is one of the most important factors to achieve high carrier mobility<sup>1–13</sup> toward high-end devices such as radiofrequency identifier (RF-ID) tags, sensors, and energy harvesting devices. Toward such electronics, solution processability and chemical and thermal stability are additional requirements for decreasing total costs of material purifications and device fabrications. To accomplish these requirements, there are several reports regarding designs of OSC molecules. A series of thienothiophene-based OSCs has been developed among which alkyl-substituted-[1]-benzothieno[3,2-*b*][1]benzothiophenes ( $C_n$ -BTBT)<sup>2</sup> and -dinaphtho[2,3-*b*:2',3'-*f*]thieno[3,2-*b*]thiophene ( $C_n$ -DNTT) exhibit high chemical stability under ambient conditions and charge carrier mobility more than  $10 \text{ cm}^2 \text{ V}^{-1} \text{ s}^{-1}$  in solution-processed films.<sup>2,5,8</sup> In particular, the  $\pi$ -

extended  $C_n$ -DNTT exhibits poor solubility at room temperature, resulting in a disadvantage for solution processes below  $100 \text{ }^\circ\text{C}$ .<sup>5</sup> Although less  $\pi$ -extended  $C_n$ -BTBTs exhibit good solubility in common organic solvents at room temperature, they possess relatively deep energy levels of the highest occupied molecular orbital (HOMO) as a p-type OSC, often resulting in large operating voltages in field-effect transistors (FETs) with gold and carbon electrodes. Recently, we also developed conceptually new oxygen- and sulfur-bridged V-shaped binaphthalene  $\pi$ -electron cores ( $\pi$ -cores), dinaphtho[2,3-*b*:2',3'-*d*]furan (DNF-V) and -thiophene (DNT-V)

Received: May 20, 2020



(Figure 1a).<sup>6,14–18</sup> Both V-shaped derivatives showed (1) high chemical stability under ambient conditions due to deep

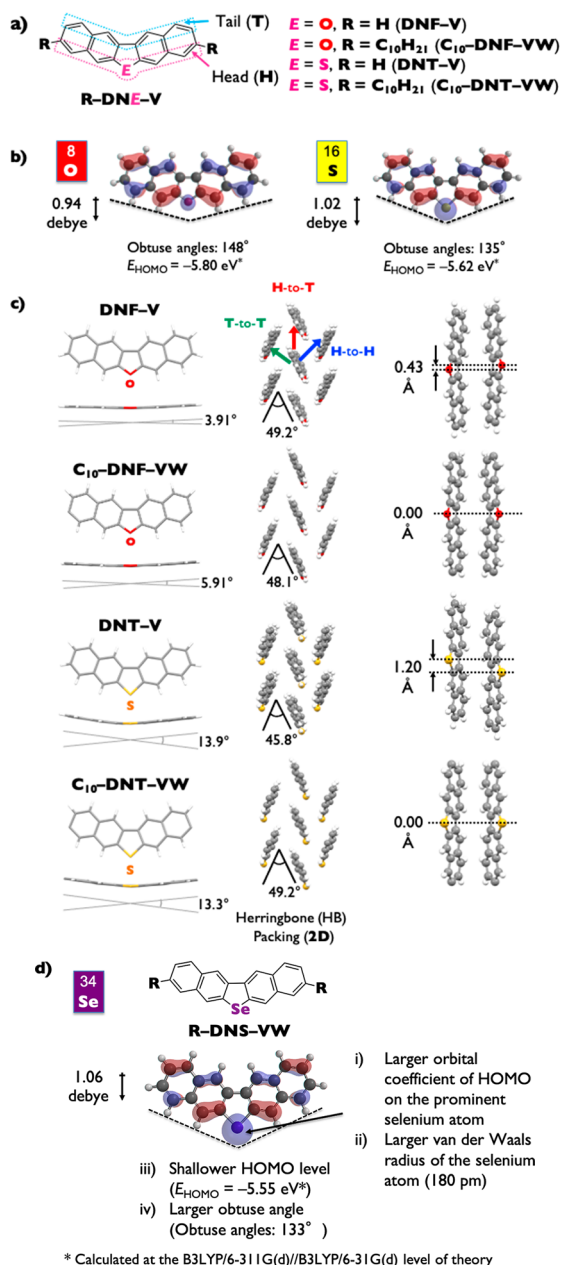


**Figure 1.** (a) Chemical structures of oxygen- and sulfur-bridged V-shaped derivatives, DNF-V and DNT-V. (b) HOMO coefficients and their levels, molecular shape, and dipole moments (calculated at the B3LYP/6-311G(d)//B3LYP/6-31G(d) level of theory). (c) Molecular and aggregated structures in single crystals, and molecular displacements of tail-to-tail (T-to-T) directions for DNF-V and DNT-V derivatives. (d) Molecular design of selenium-bridged π-electron core R-DNS-VW in this work.

HOMO levels of  $<-5.0$  eV to resist oxidation by ambient O<sub>2</sub>,<sup>19</sup> (2) suitable solubility in common organic solvents owing to their intramolecular dipole moments (Figure 1b),<sup>20</sup> (3) high thermal stability without any reactive chemical bonds, and (4) charge carrier mobility equal or superior to currently used amorphous silicon semiconductors (0.5–1.0 cm<sup>2</sup> V<sup>-1</sup> s<sup>-1</sup>). Comprehensive studies of their decyl-substituted derivatives, 3,9-didecyldinaphtho[2,3-*b*:2',3'-*d*]furan (C<sub>10</sub>-DNF-VW)

and -thiophene (C<sub>10</sub>-DNT-VW), suggested that the central bridging elements and the lateral alkyl side chains conclusively affect their molecular geometries, aggregated structures, and semiconducting properties.<sup>6,7,21</sup> Unlike the reported conventional chalcogen-bridged π-cores, V-shaped π-cores form unique bent molecular structures (bent angles between naphthalenes: 3.91–13.9°) in the solid state depending on the bridged elements and substituents (Figure 1c). The long linear alkyl chains could finely tune their herringbone (HB)-packing motif by multipoint van der Waals interactions to eliminate displacements along molecular longitudinal axis while unsubstituted DNF-V and DNT-V show larger displacements of 0.43 and 1.20 Å, respectively (Figure 1c). As a result, C<sub>10</sub>-DNF-VW and C<sub>10</sub>-DNT-VW exhibited elevated carrier mobility up to 1.3 and 6.5 cm<sup>2</sup> V<sup>-1</sup> s<sup>-1</sup>,<sup>6,14</sup> respectively, due to effective intermolecular orbital overlaps.

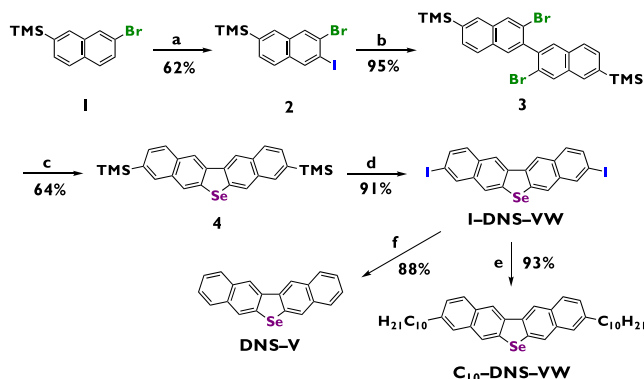
In this work, we focused on selenium-bridged V-shaped π-core, dinaphtho[2,3-*b*:2',3'-*d*]selenophene (DNS-V) (Figure 1d). In contrast to DNF-V and DNT-V, DNS-V exhibits several advantages as follows: (1) larger HOMO coefficients on the prominent selenium atom than others, (2) improved intermolecular orbital overlaps in aggregated structures, leading to higher carrier mobility, and (3) shallower HOMO level to afford smaller operating voltage (threshold voltage) for transistors. Hitherto, small molecule-type selenium-containing OSCs were reported by several groups.<sup>3,22–29</sup> Among them, benzo[1,2-*b*:4,5-*b'*]diselenophenes (BDSs) and [1]-benzoselenopheno[3,2-*b*][1]benzoselenophenes (BSBSs) possessing large HOMO coefficients on selenium atoms have also been developed to aim for enhancement of intermolecular orbital overlaps. However, they unexpectedly exhibited device performances comparable or lower than that of sulfur counterparts. Therefore, sulfur-containing OSCs are still a main player in the field of high performance OSCs. Here, compared with the reported selenium-containing OSCs, it is expected that the prominent selenium atom as well as the unique feature of bent molecular structure in the aggregated form in a V-shaped π-core can generate new features as OSCs.

Herein DNS-V and its decyl-substituted derivative (3,9-didecyldinaphtho[2,3-*b*:2',3'-*d*]selenophene, C<sub>10</sub>-DNS-VW) are studied comprehensively. DNS-V and C<sub>10</sub>-DNS-VW were readily synthesized by a modified methodology of the reported case of sulfur-bridged V-shaped derivatives.<sup>5</sup> Surprisingly, DNS-V and C<sub>10</sub>-DNS-VW showed one order higher solubility compared to the reported oxygen- and sulfur-bridged V-shaped counterparts in commonly used organic solvents. Unlike all of other V-shaped derivatives with 2D HB packing motifs (2D motifs) (Figure 1c), interestingly, depending on crystal growth conditions in solutions, C<sub>10</sub>-DNS-VW forms a one-dimensionally π-stacked packing motif (1D motif) and a 2D motif. Its thin film grown by either the vacuum-deposited or the solution-crystallized process affords only the 2D motif. Once the 1D motif is heated over 80 °C, the 2D motif forms and is maintained in the subsequent cooling process. The 1D motif is obtained again after exposure of the 2D motif to certain organic solvents. This result implies that 1D and 2D motifs of long alkyl-substituted C<sub>10</sub>-DNS-VW are synergistically induced by the total balance of the C–H⋯π and Se⋯π interactions. Using solution-grown single-crystalline films, C<sub>10</sub>-DNS-VW exhibits carrier mobility up to 11 cm<sup>2</sup> V<sup>-1</sup> s<sup>-1</sup> with suitable transistor stability under ambient conditions for more than two months.

## 2. RESULTS AND DISCUSSION

**2.1. Synthesis.** First, a modular synthetic protocol was developed toward DNS–V derivatives as shown in Scheme 1.

### Scheme 1. Synthesis of Unsubstituted DNS–V and C<sub>10</sub>–DNS–VW<sup>a</sup>



<sup>a</sup>Reagents and condition: (a) (1) *t*-Bu<sub>2</sub>Zn(TMP)Li, THF, –10 °C, 10 h, (2) I<sub>2</sub>, –10 °C, 2 h, (b) (1) *i*-PrMgBr, (2) ZnCl<sub>2</sub>, LiCl, –78 °C, 30 min, (3) Compound 2, Pd(PPh<sub>3</sub>)<sub>4</sub>, THF/NMP, rt, 16 h, (c) (1) *n*-BuLi, Et<sub>2</sub>O, –78 to 0 °C, 1 h, (2) SeCl<sub>2</sub>, –78 °C, 1 h, (d) ICl, CH<sub>2</sub>Cl<sub>2</sub>, –78 to 0 °C, 2 h, (e) *n*-C<sub>10</sub>H<sub>21</sub>MgBr, ZnCl<sub>2</sub>, LiCl, PdCl<sub>2</sub>(dppf)·CH<sub>2</sub>Cl<sub>2</sub>, toluene, 70 °C, 12 h. (f) PdCl<sub>2</sub>(dppf), TMEDA, NaBH<sub>4</sub>, THF, rt, 5 h.

Starting from trimethylsilyl (TMS)-substituted 2-bromonaphthalene derivative **1**, an ortho-metalation was performed using *t*-Bu<sub>2</sub>Zn(TMP)Li (TMP: 2,2,6,6-tetramethylpiperidine) as a zinc base,<sup>30–32</sup> because metalation by other bases such as lithium diisopropylamide (LDA) and LiTMP resulted in complex mixtures, likely caused by debromination after the formation of deprotonated species. The reaction of compound **1** with *t*-Bu<sub>2</sub>Zn(TMP)Li produced a zincate intermediate (>90% deuterium incorporation determined by <sup>1</sup>H NMR), which was treated with iodine to generate iodinated compound **2** in 62% yield. After the treatment of compound **2** with Grignard reagent followed by transmetalation with zinc, Negishi coupling reaction produced the dibromonaphthalene derivative **3**. Subsequently, the dilithio intermediate was generated by *n*-BuLi, which was trapped by selenium dichloride<sup>33</sup> to produce TMS-substituted DNS–V (**4**). After conversion into iodinated DNS–V (I–DNS–VW), the introduction of a decyl group as a synthetic module afforded the target compound, C<sub>10</sub>–DNS–VW, in high yield. DNS–V can be synthesized by the reported hydrodehalogenation.<sup>34</sup> This synthetic protocol can also be applicable to the synthesis of our previously developed DNT–V congeners by replacement of reagent from selenium dichloride to sulfur. Thus, utilizing the developed modular synthetic protocol, a wide variety of selenium-bridged V-shaped derivatives were successfully synthesized by coupling reactions, which will be reported elsewhere.

**2.2. Thermal Stability Test and Determination of Ionization Potentials.** Thermal properties and ionization potentials (IPs) were evaluated for DNS–V and C<sub>10</sub>–DNS–VW along with V-shaped derivatives (DNF–V, C<sub>10</sub>–DNF–VW, DNT–V, and C<sub>10</sub>–DNT–VW) for comparisons. Thermogravimetric (TG) analysis revealed that no thermal decomposition was observed for DNS–V and C<sub>10</sub>–DNS–VW, similar to V-shaped derivatives (Figure 2a and Figures S1 and

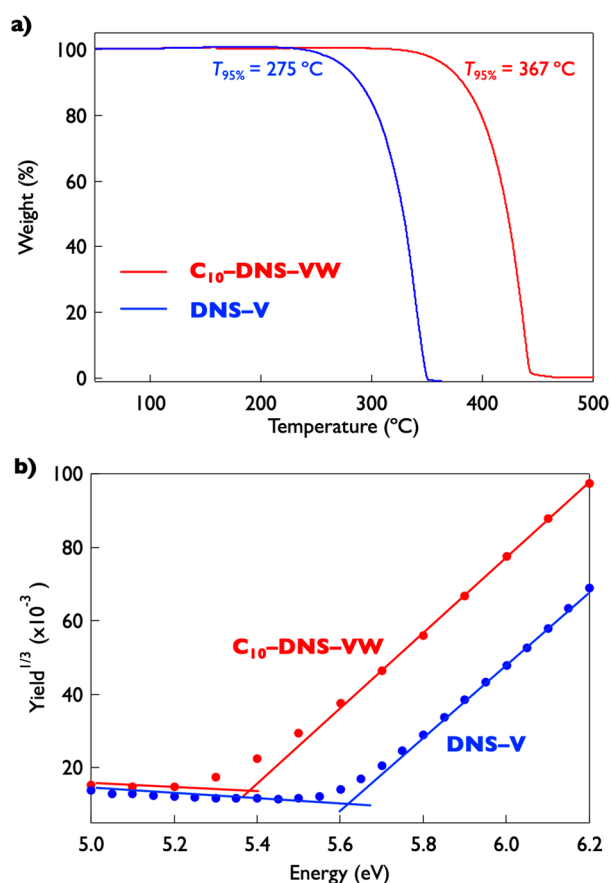


**Figure 2.** (a) Thermogravimetric analysis and (b) photoelectron yield spectroscopy of DNS–V and C<sub>10</sub>–DNS–VW.

S2). This indicates that device-grade materials can be easily prepared by repeated sublimation. The IPs of DNS–V and C<sub>10</sub>–DNS–VW were estimated by photoelectron yield spectroscopy (PYS) which were determined to be 5.63 and 5.39 eV, suggesting that DNS–V derivatives are also promising candidates as air-stable p-type OSCs (Figure 2b).<sup>35</sup> As expected, DNS–V derivatives exhibit the smallest IPs among a series of V-shaped derivatives (5.93 eV, 5.73 eV, 5.72 eV, and 5.44 eV for DNF–V, C<sub>10</sub>–DNF–VW, DNT–V, and C<sub>10</sub>–DNT–VW, respectively), and the trend is well consistent with the calculated results (Figure 1b,d and Table S3).

**2.3. Aggregated Structures.** To determine molecular and aggregated structures of DNS–V and C<sub>10</sub>–DNS–VW, single crystals were grown from either physical-vapor transport or recrystallization techniques. Both DNS–V and C<sub>10</sub>–DNS–VW single crystals were obtained as colorless needles whose structural data were successfully collected by single crystal X-ray diffraction (SC-XRD) analysis (Figure S5 and 3a for DNS–V and C<sub>10</sub>–DNS–VW). Although sterically less demanding oxygen- and sulfur-bridged DNF–V and DNT–V form bent molecular structures and HB packing motifs (Figure 1c), DNS–V having the much larger selenium atom does not assume HB packing but rather a slipped one-dimensional (1D)  $\pi$ -stacking motif showing an almost planar molecular structure (the bent angle between the two naphthalene planes is 2.25°) (Figure S5a). In C<sub>10</sub>–DNS–VW colorless crystals (C<sub>10</sub>–DNS–VW-colorless), the molecular structure of DNS–V unit also assumes almost planar geometry with the bent angle of 1.53° (Figure 3a), which is

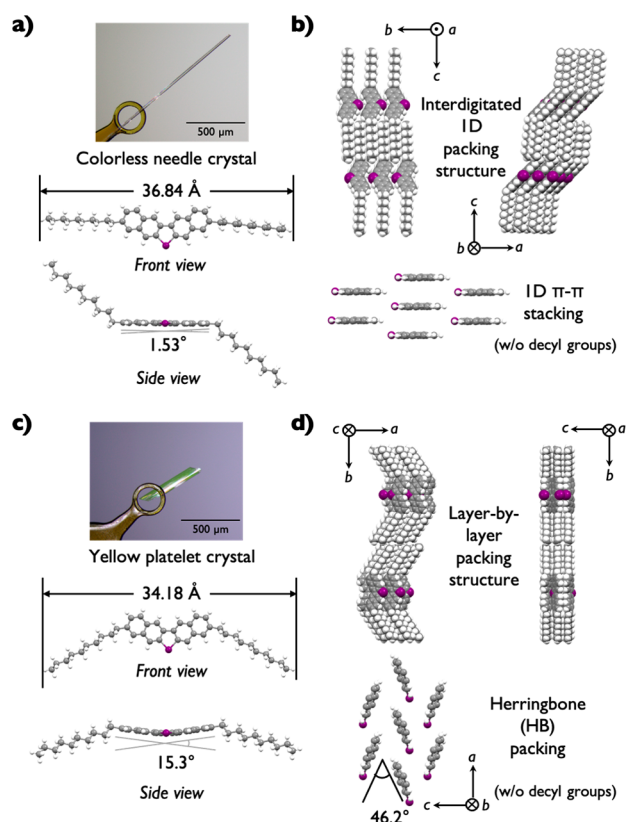


**Figure 3.** Molecular structure and aggregated structure of (a, b)  $C_{10}$ -DNS-VW-colorless and (c, d)  $C_{10}$ -DNS-VW-yellow phases in single-crystal structures.

different from DNF-V and DNT-V derivatives (Figure 1c).  $C_{10}$ -DNS-VW-colorless assembles the face-to-face 1D  $\pi$ -stacking motif with interdigitated alkyl chains (Figure 3b). Surprisingly, during quick recrystallization and reprecipitation from alcohol solvents,  $C_{10}$ -DNS-VW was obtained as yellow microcrystals and powders. By a careful recrystallization, we successfully obtained yellow platelet single crystals and performed the SC-XRD analysis, as shown in Figure 3c,d. In the  $C_{10}$ -DNS-VW yellow platelet crystals ( $C_{10}$ -DNS-VW-yellow), the molecular structure of the  $\pi$ -core assumes a bent molecular structure with the bent angle of 15.3°, resembling geometries of other bent-shaped derivatives (Figure 1c).  $C_{10}$ -DNS-VW-yellow forms the 2D HB packing motif, which is preferable for carrier transport.<sup>36</sup> The bent angles between the two naphthalene units becomes larger in the order of oxygen, sulfur, and selenium owing to the increase in van der Waals radius of chalcogens. Thus, such unique crystal polymorphism of  $C_{10}$ -DNS-VW could be synergistically induced by the steric repulsion force between adjacent selenium atoms and the multiple van der Waals interactions between long decyl side chains, while such structural and color changes are not observed in the case of the furan or thiophene analogues due to less steric effect.

**2.4. Aggregation Behavior.** In the course of melting point measurements, the following phenomena of  $C_{10}$ -DNS-VW were observed in solid state. Once the colorless solid was heated to approximately 80 °C, it turned to the yellow solid and maintained its color upon cooling to room temperature (Figure 4a). The phenomena were further investigated by differential scanning calorimetry (DSC) (Figure 4b and Figure S6) together with variant temperature X-ray diffraction (VT-XRD)

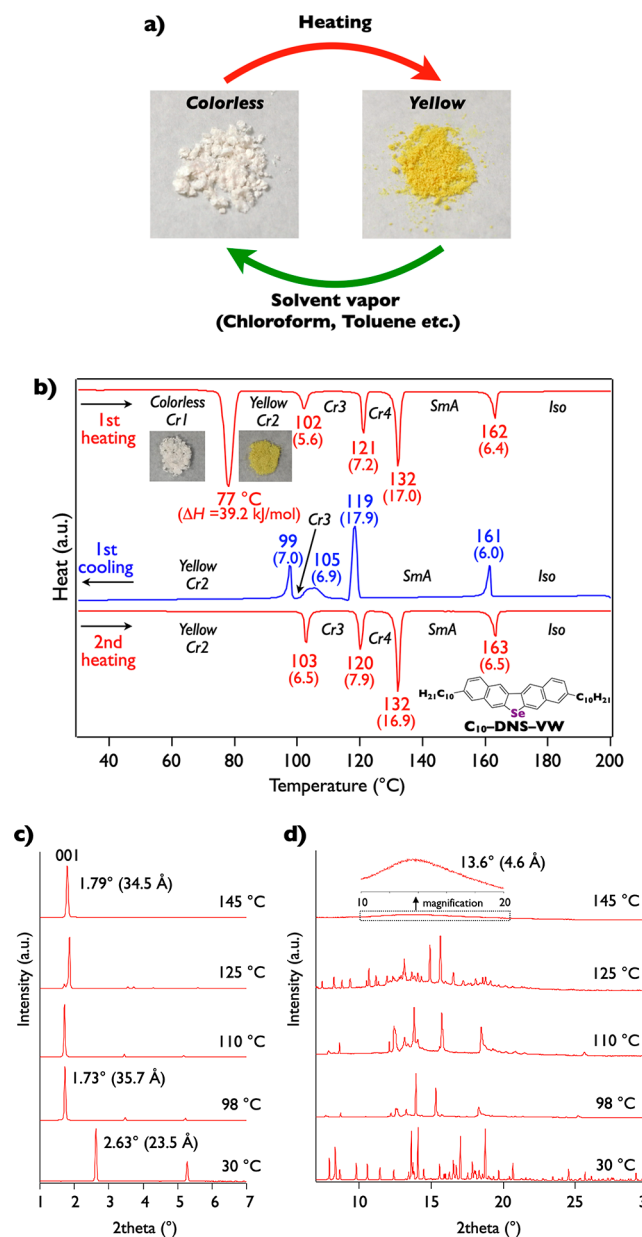


**Figure 4.** (a) Transitions between colorless and yellow phases by means of heating and solvent vapor. (b) DSC measurement of  $C_{10}$ -DNS-VW in the range from room temperature to 200 °C in the first scan at the rate of 5 K/min under a nitrogen flow. (c, d) Variant temperature XRD patterns of  $C_{10}$ -DNS-VW on heating: (c) in the small-angle region and (d) in the wide-angle region.

measurements using synchrotron radiation<sup>37</sup> with the wavelength at 1.08 Å (Figure 4c,d and Figures S8-S10). In the first heating process, a large endothermic peak ( $\Delta H = 39.2$  kJ/mol) was observed at 77 °C. In this process, the VT-XRD profile dramatically changed corresponding to the colorless-to-yellow-crystal transformation. Notably, the lowest angle diffraction peak highly shifted from 2.63° (measured at 30 °C) to 1.73° (measured at 98 °C) corresponding to the  $d$ -spacing change from 23.5 to 35.7 Å, which is identical to a half of the cell axis length along the molecular long axis of  $C_{10}$ -DNS-VW-colorless- and -yellow-phases, 46.87 and 70.15 Å, respectively. Note that the yellow phase does not convert back to colorless by cooling to room temperature (Figures S8 and S10), which indicates that the first phase-transition is thermally

irreversible. Interestingly, the yellow phase turned the colorless one back again by exposure to organic solvents, as revealed by powder XRD measurements (Figure S12). That is, two kinds of solid phases could be reversibly transformed upon external stimuli. The period of color change depends on the choice of solvent. For example, in the case of good solvents such as chloroform and toluene vapor, the color immediately changed within a few seconds, while in the cases of relatively poor solvents such as acetone and hexane, the color change was on the order of minutes. In contrast, acetonitrile and 2-propanol, which are poor solvents for C<sub>10</sub>-DNS-VW, caused little to no change in color for a long period. With this experimental knowledge in hand, it is inferred that the colorless phase is more energetically stable than the yellow one. Such a drastic phase transition with the change of color<sup>38</sup> observed in C<sub>10</sub>-DNS-VW is unique among the V-shaped derivatives.

During further heating of C<sub>10</sub>-DNS-VW over 90 °C, four additional phase transition peaks were observed at 102 °C, 121 °C, 132 °C, and 162 °C. Although there exist peak shifts due to supercooling, these four transition peaks were also detected during the cooling process, indicating their reversible phase transitions. XRD patterns measured at 110 °C and 125 °C show multiple sharp peaks even in wide-angle regions, indicating the highly ordered-assembled structures of C<sub>10</sub>-DNS-VW. In contrast, over 132 °C, C<sub>10</sub>-DNS-VW was found to form a mobile and ordered liquid-crystalline state. As measured at 145 °C, only one diffraction peak was observed in the small angle region with a *d* spacing of 34.5 Å (for instance, the molecular length in the C<sub>10</sub>-DNS-VW-yellow crystal along the longitudinal axis is 34.18 Å, as shown in Figure 3c), whereas the wide-angle region around 13.6° (4.6 Å) shows a diffused halo, ascribing to the diffraction from the disordered alkyl chains. The polarizing optical microscopic image at that temperature shows a fan-shaped texture, indicating that C<sub>10</sub>-DNS-VW forms a smectic A phase in the temperature region from 132 °C to 162 °C (Figure S11). C<sub>10</sub>-DNS-VW ultimately transforms into the isotropic phase over 162 °C.

**2.5. Physicochemical Properties and Chemical Stability Test in Solution and Thin Film.** To clarify physicochemical properties and chemical stability of C<sub>10</sub>-DNS-VW, its UV-vis spectra in solution were measured under ambient conditions. Among a series of V-shaped derivatives, C<sub>10</sub>-DNS-VW has an absorption spectrum similar to that of C<sub>10</sub>-DNT-VW, and they are red-shifted compared to C<sub>10</sub>-DNF-VW. The effect of chalcogen substitution on the absorption properties of V-shaped derivatives in both of the single molecular states and aggregated states is saturated around sulfur and selenium atoms (Figure 5a,b). Furthermore, on the basis of time-dependent spectra of C<sub>10</sub>-DNS-VW in both solution and thin-film states, no spectral change was detected over 1 week, indicating its excellent chemical stability under ambient conditions (Figures S14 and S15). The vacuum-deposited thin film corresponds to the yellow phase, which is determined by thin-film XRD (Figure S20).

**2.6. Solubility.** The solubility of C<sub>10</sub>-DNS-VW was determined using several organic solvents at room temperature. C<sub>10</sub>-DNS-VW shows very high solubility in the range of 0.74–1.97 wt % in chloroform, toluene, and *o*-dichlorobenzene (*o*DCB) (1.97 wt % in chloroform, 0.74 wt % in toluene, and 1.73 wt % in *o*-DCB) despite the extensively fused  $\pi$ -system. C<sub>10</sub>-DNF-VW and C<sub>10</sub>-DNT-VW exhibit much lower solubility of below 0.1 and 0.6 wt % in chloroform

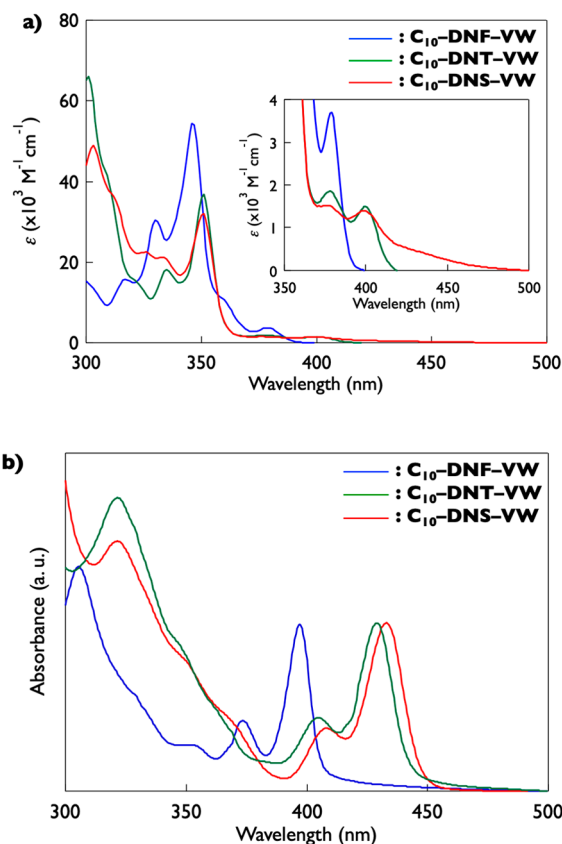


**Figure 5.** (a) Absorption spectra of C<sub>10</sub>-DNF-VW (blue line), C<sub>10</sub>-DNT-VW (green line), and C<sub>10</sub>-DNS-VW (red line) in comparison in 1,2-dichloroethane solution ( $c = 1.0 \times 10^{-5}$  M) at room temperature. (b) Absorption spectra of C<sub>10</sub>-DNF-VW (blue line), C<sub>10</sub>-DNT-VW (green line), and C<sub>10</sub>-DNS-VW (red line) in ca. 100 nm thin film.

under the same conditions, respectively. C<sub>10</sub>-DNS-VW-yellow and -colorless solids exhibited the same solubility, because C<sub>10</sub>-DNS-VW-yellow solids were fully converted into the C<sub>10</sub>-DNS-VW-colorless form upon exposure to good solvents. Considering that C<sub>10</sub>-DNF-VW and C<sub>10</sub>-DNT-VW do not show any polymorphisms, this result might indicate that the high solubility of C<sub>10</sub>-DNS-VW mainly originates from the unique phase transition behavior from C<sub>10</sub>-DNS-VW-yellow to C<sub>10</sub>-DNS-VW-colorless in good solvents, which later forms 1D aggregated structure with weaker intermolecular interactions (Figure S17). Furthermore, the slightly larger dipole moment of DNS-V (1.06 debye) compared with those of DNF-V (0.94 debye) and DNT-V (1.02 debye) might also play a role in improved solubility (Figure 1b,d).<sup>20</sup>

**2.7. Carrier Transport Capability Analyzed by Theoretical Calculations.** Based on the packing structure, intermolecular electronic couplings were estimated by the transfer integral (*t*) for holes using the dimer approach<sup>39</sup> at the PBE/6-31G(d) level of theory. On the basis of calculations based on the molecular structures in single crystals, C<sub>10</sub>-DNS-VW-yellow, C<sub>10</sub>-DNF-VW, and C<sub>10</sub>-DNT-VW exhibit small energetic differences between HOMO and next HOMO (NHOMO). The small differences suggest that *t* values of HOMO-HOMO and NHOMO-NHOMO should be taken into account, but *t* values between HOMO-NHOMO were estimated to be either zero or

negligibly small unlike recently reported BTBT derivatives.<sup>40</sup> The calculation results for HOMO–HOMO and NHOMO–NHOMO of C<sub>10</sub>–DNS–VW–colorless and –yellow are summarized in Figure 6a,b. The C<sub>10</sub>–DNS–VW–colorless

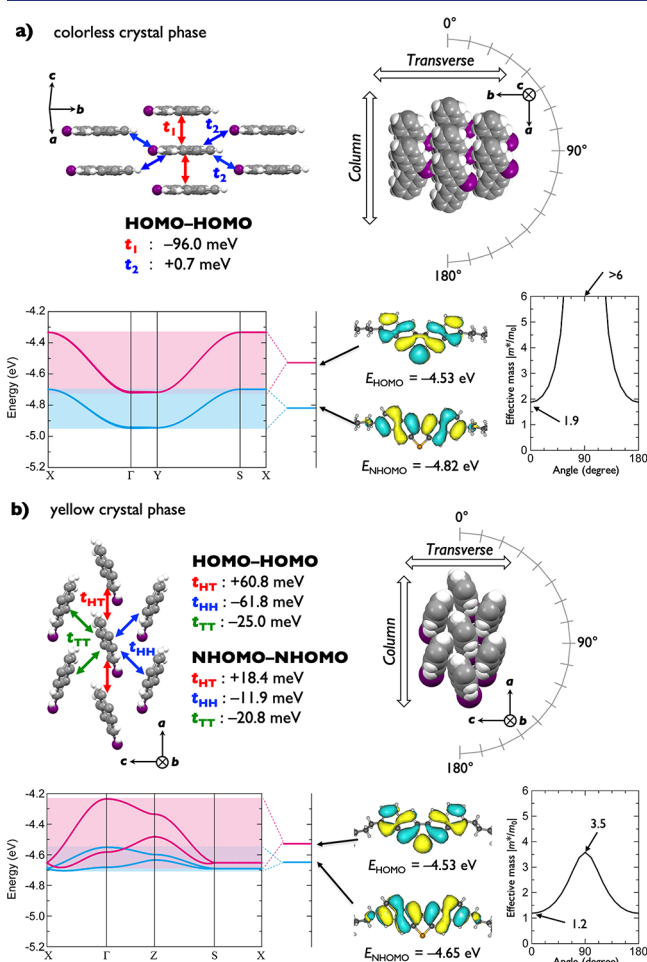


**Figure 6.** Calculation results of (a) C<sub>10</sub>–DNS–VW–colorless and (b) C<sub>10</sub>–DNS–VW–yellow crystal phases. Packing structures with transfer integrals of HOMO–HOMO and NHOMO–NHOMO, electronic band structure with  $E_{\text{HOMO}}$  and  $E_{\text{NHOMO}}$ , and effective masses ( $a$ – $b$  and  $a$ – $c$  planes) depending on the angle from the column direction (calculated at the PBEPBE/6-31G(d) level of theory).

exhibits typical features of 1D charge-transport with a large negative value of  $-96$  meV and very small positive value of  $+0.7$  meV between HOMOs for  $t_1$  and  $t_2$  (in the lateral directions). On the other hand, C<sub>10</sub>–DNS–VW–yellow exhibits large positive values of  $+61$  meV ( $t_{\text{HT}}$ ) in the column direction and two negative values of  $-62$  meV ( $t_{\text{HH}}$ ) and  $-25$  meV ( $t_{\text{TT}}$ ) in transverse directions, and  $+18$ ,  $-12$  and  $-21$  meV between NHOMOs for  $t_{\text{HT}}$ ,  $t_{\text{HH}}$ , and  $t_{\text{TT}}$ , respectively.

To quantitatively understand the carrier transport capability, the electronic band structures were also calculated via the periodic boundary condition at the same level as the estimation of  $t$  values. Theoretically, the hole mobility is inversely proportional to  $m^*$ , as described in the following equation:  $\mu = q\tau/m^*$  ( $\mu$ : mobility,  $q$ : carrier charge,  $\tau$ : relaxation time,  $m^*$ : effective mass). The  $m^*$  values were estimated from the band dispersion on top of the bands. Figure 6 and Table S4 summarize their effective masses for holes. For C<sub>10</sub>–DNS–VW–colorless, effective masses (contributed by HOMO) were

evaluated to be as small as  $1.9m_0$  in the  $a$ -axis but more than  $6m_0$  in the  $b$ -axis direction, indicating anisotropic 1D charge transport behavior (Figure 6a). On the other hand, for the 2D HB motif of C<sub>10</sub>–DNS–VW–yellow, effective masses were well balanced and estimated to be  $1.2m_0$  in the column direction ( $m_{\parallel}^*$ ) and  $3.5m_0$  in the transverse direction ( $m_{\perp}^*$ ) (Figure 6b). The values are more isotropic, and small or similar compared with those of C<sub>10</sub>–DNF–VW ( $m_{\parallel}^* = 5.2m_0$  and  $m_{\perp}^* = 1.8m_0$ ) and C<sub>10</sub>–DNT–VW ( $m_{\parallel}^* = 1.5m_0$  and  $m_{\perp}^* = 2.7m_0$ ) (Figures S18 and S19) showing the highest mobility up to  $1.3$  and  $6.5$  cm<sup>2</sup> V<sup>-1</sup> s<sup>-1</sup>, respectively.<sup>6,14</sup> Furthermore, the column direction of C<sub>10</sub>–DNS–VW–yellow is preferable for transport to the transverse direction.

## 2.8. FET Performances and Stability under Ambient Conditions.

To evaluate FET performance for DNS–V and C<sub>10</sub>–DNS–VW, their thin films on self-assembled monolayer (SAM)-treated Si/SiO<sub>2</sub> substrate were prepared in the form of both polycrystalline and single crystalline by means of vacuum deposition, manual lamination, or solution process by the edge-casting method.<sup>41</sup> For DNS–V, manually laminated single-crystal OFETs were evaluated at ambient conditions. The laminated single-crystal transistor exhibits hole mobility up to  $0.11$  cm<sup>2</sup> V<sup>-1</sup> s<sup>-1</sup> (Figure S22). For C<sub>10</sub>–DNS–VW, vacuum-deposited polycrystalline and solution-grown single crystalline thin-film FETs exhibit hole mobility up to  $3.2$  (substrate temperatures:  $90$  °C and  $115$  °C, thickness of OSCs:  $40$  nm) and  $11$  cm<sup>2</sup> V<sup>-1</sup> s<sup>-1</sup>, respectively (Figure S24 and S25 and Figure 7a–d). The maximum value of single crystalline FET is indeed superior to those of oxygen- and sulfur-bridged counterparts. Also, its threshold voltage ( $V_{\text{th}}$ ) is reduced to as small as  $-30$  to  $-15$  V, compared to C<sub>10</sub>–DNT–VW ( $V_{\text{th}} = -40$  V) with the same device structure, resulting from the smaller ionization potential of C<sub>10</sub>–DNS–VW (Table 1). The device stability of C<sub>10</sub>–DNS–VW single-crystal OFET was investigated against atmospheric stress. No critical decreases in hole mobility ( $\mu_{\text{h}}$ ) and  $V_{\text{th}}$  were detected over two months (Figure 7e). Regarding the initial deterioration, this may be caused by the evaporation of the residual solvent at the crystal–substrate interface or in the crystal.<sup>42</sup>

## 2.9. Thin-Film Morphology and Molecular Dynamic Simulations.

Out-of-plane XRD measurements of both the polycrystalline and the single-crystalline thin film indicated that C<sub>10</sub>–DNS–VW forms layer-by-layer lamella structure, judging from  $(0\ 4\ 0)$ ,  $(0\ 6\ 0)$ ,  $(0\ 8\ 0)$ , and  $(0\ 10\ 0)$  diffraction with a calculated interlayer  $d$ -spacing of about  $70.6$ – $70.8$  Å (Figure S20). The value is in good accordance with the lattice constant of the yellow phase ( $70.15$  Å) in the molecular long axis. This is probably because the interdigitated alkyl chain assembly in the C<sub>10</sub>–DNS–VW–colorless crystal structure is energetically unpreferable in the two-dimensional surface. To investigate the stable structure of thin films composed of C<sub>10</sub>–DNT–VW–colorless and –yellow, molecular dynamics (MD) simulations for the system of thin films on the  $\beta$ -PTS-treated SiO<sub>2</sub> surface were carried out, respectively (Figure 8). For the thin films of C<sub>10</sub>–DNT–VW–colorless on the substrate, the molecular alignments of the top and bottom layers were deformed during  $5$  ns of the MD run (Figure 8a). However, the thin films of C<sub>10</sub>–DNT–VW–yellow on the substrate were unchanged from the bulk crystal structure at the initial state, and the thickness of two layers calculated from the structure obtained by MD simulation was about  $70$  Å. This strongly supports the

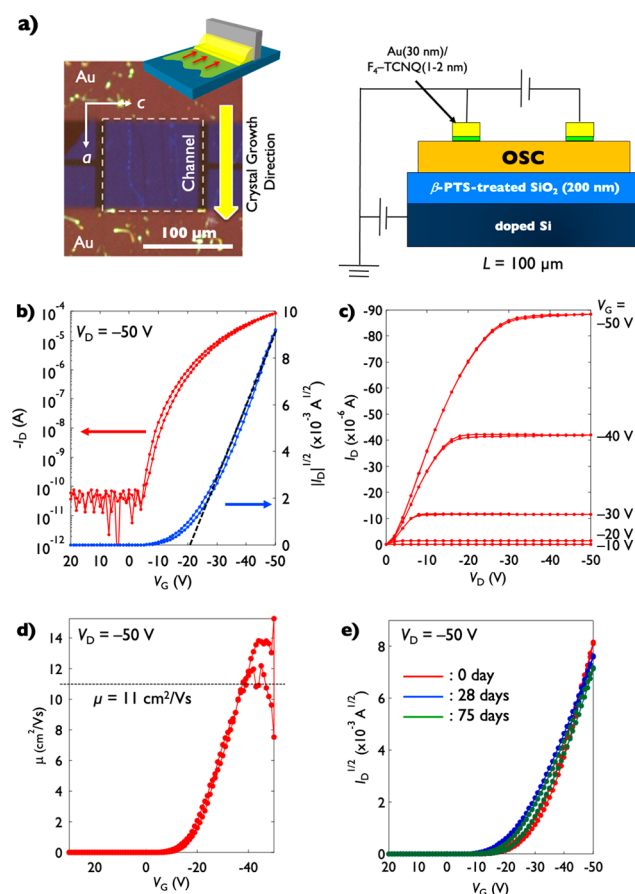


**Figure 7.** (a) A polarized microscopy image and a device illustration, (b) transfer and (c) output characteristics, (d) effects of  $V_G$  on  $\mu_{\text{tr}}$ , and (e) change of the transfer curve on storage under ambient conditions of a  $C_{10}$ -DNS-VW solution-grown single-crystal FET: channel length ( $L$ ) = 100  $\mu\text{m}$ ; channel width ( $W$ ) = 100  $\mu\text{m}$ ; gate electrode ( $G$ ) =  $n++\text{-Si}$ ; insulator ( $\text{Ins}$ ) =  $\text{SiO}_2$  (200 nm,  $C_i = 16.8 \text{ nF cm}^{-2}$ ); source ( $S$ ) and drain ( $D$ ) electrodes =  $F_4\text{-TNCQ}(1\text{-}2 \text{ nm})/\text{Au}$  (30 nm).

fact that  $C_{10}$ -DNT-VW-yellow preferably forms layer-by-layer lamella structure on the substrate (Figure 8b).

To determine the crystal growth direction of solution-grown single-crystalline films, XRD measurements were performed using synchrotron radiation with the wavelength at 1.000 and 0.689  $\text{\AA}$  for out-of-plane and in-plane measurements, respectively (Figure 9). The out-of-plane XRD pattern shows three reflections at 34.7, 17.5, and 11.6  $\text{\AA}$  (Figure 9b), while

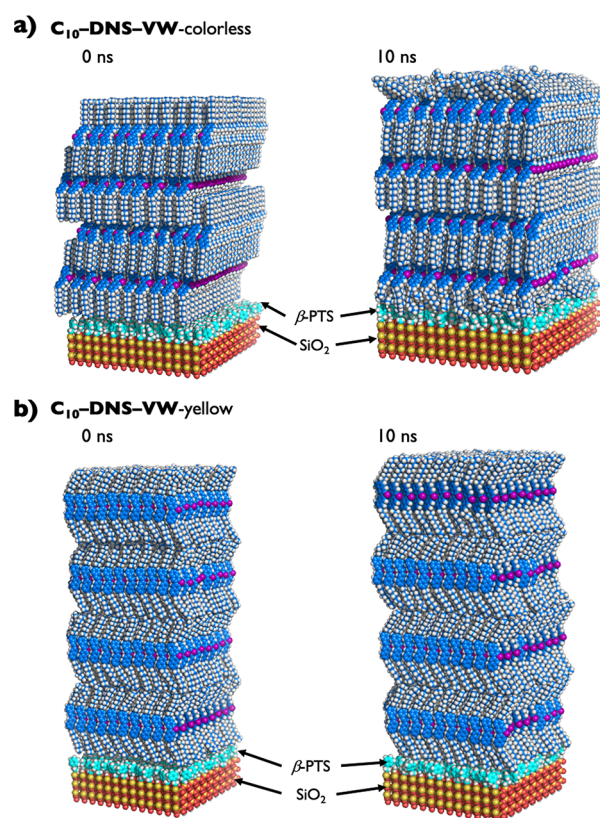


**Figure 8.** Molecular dynamics of (a)  $C_{10}$ -DNS-VW-colorless and (b)  $C_{10}$ -DNS-VW-yellow phases on the  $\beta$ -PTS-treated  $\text{SiO}_2$  surface.

some indicative reflections were detected at 3.89 and 3.31  $\text{\AA}$  in the in-plane XRD pattern (Figure 9c). Out-of-plane reflections correspond to diffraction from (0 2 0), (0 4 0), and (0 6 0) planes of the yellow phase whereas in-plane peaks correspond to (0 0 2) and (1 0 2) planes, implying that thin films prepared on the substrate form 2D HB packing structures and a conduction  $a$ - $c$  plane parallel to the substrate. Furthermore, the column  $a$  direction, showing potentially high mobility, is almost parallel to the crystal growth direction.

### 3. CONCLUSION

In summary, we demonstrated that a selenium-bridged V-shaped  $\pi$ -core functionalized by long alkyl chains,  $C_{10}$ -DNS-VW, possesses two types of aggregated forms: a thermally stable colorless phase having high solubility and a metastable yellow phase preferably forming on the surface and showing

**Table 1. Summary of Transistor Performance in Single Crystal and Polycrystalline Thin Films of  $C_{10}$ -DNS-VW-Yellow,  $C_{10}$ -DNS-VW-Colorless, and DNS-V**

material	film for FET	mobility ( $\text{cm}^2 \text{V}^{-1} \text{s}^{-1}$ )		$V_{\text{th}}$ (V)	$I_{\text{on/off}}$
		$\mu_{\text{ave}}^a$	$\mu_{\text{max}}$		
$C_{10}$ -DNS-VW-yellow	single crystal	$7.0 \pm 2.1$	11	-30 to -15	$10^6$
	polycrystalline ( $T_{\text{sub}} = \text{rt}$ )	$1.0 \pm 0.05$	1.1	-30 to -25	$10^5$
	polycrystalline ( $T_{\text{sub}} = 90 \text{ }^\circ\text{C}$ )	$2.3 \pm 0.6$	3.2	-30 to -25	$10^5$
	polycrystalline ( $T_{\text{sub}} = 115 \text{ }^\circ\text{C}$ )	$2.8 \pm 0.4$	3.2	-30 to -25	$10^5$
$C_{10}$ -DNS-VW-colorless	single crystal	n.a. <sup>b</sup>	$3.0 \times 10^{-4c}$	n.a. <sup>d</sup>	15
DNS-V	single crystal	$0.088 \pm 0.13$	0.11	-70 to -50	$10^3$

<sup>a</sup>The average values (average value  $\pm$  standard deviation) are evaluated from 5 to 10 good-looking devices. <sup>b</sup>The value is not available because only a few devices were successfully measured. <sup>c</sup>The mobility value is just for reference because the transfer curve has large hysteresis. <sup>d</sup> $V_{\text{th}}$  is difficult to determine because the transfer curves have large hysteresis and a small on/off ratio.

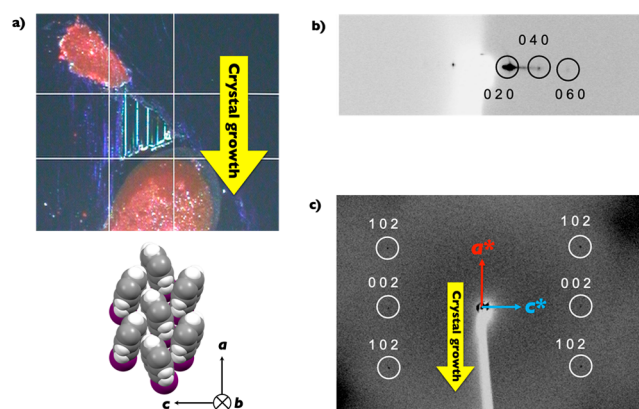


**Figure 9.** (a) A microscopic image of the solution-grown single-crystalline films on SAM-treated Si/SiO<sub>2</sub> substrates. (b) Out-of-plane (12.4 keV, 1.000 Å) and (c) in-plane (18.0 keV, 0.689 Å) XRD patterns of single crystalline film of C<sub>10</sub>-DNS-VW.

high carrier mobility. These two phases in the form of bulk powders reversibly transform by external stimuli under conditions of thermal annealing and solvent vapor. Owing to such unique phenomena, C<sub>10</sub>-DNS-VW possesses ideal features for applicable OSCs, high solubility around 1–3 wt % in common organic solvents as a colorless phase, and a HB packing motif with preferable formation on the 2D surface and high carrier-transport ability as the yellow phase. This structural change is a unique phenomenon for a selenium-bridged V-shaped  $\pi$ -core, because our previously developed oxygen- and sulfur-bridged derivatives do not show such behavior. Thus, selenium-bridged V-shaped dinaphthalenes are a new type of OSCs having unusually high solubility, despite the highly extended  $\pi$ -electron systems, and high carrier mobility up to 11 cm<sup>2</sup> V<sup>-1</sup> s<sup>-1</sup>. The discovery of this rational functionality will open up the possibility of selenium-based OSCs for printed and flexible electronics.

## 4. EXPERIMENTAL SECTION

**4.1. Solubility Test.** To a weighed sample of roughly 5 mg was added 50  $\mu$ L of chloroform, toluene, or *o*-DCB. The resulting suspension was shaken and sonicated at room temperature until no residues remained. The total volume of solvent (mL) was converted into solubility in wt %.

**4.2. Single Crystal Data.** Single crystal diffraction data of DNS-V and C<sub>10</sub>-DNS-VW-colorless crystals were collected on a Rigaku R-Axis RAPID II imaging plate diffractometer with Mo K $\alpha$  and Cu K $\alpha$ , respectively, whereas those of C<sub>10</sub>-DNS-VW-yellow crystal were collected with synchrotron radiation ( $\lambda = 0.8026$  Å) using a hybrid photon counting detector at BL02B1 of SPring-8.

*Crystal Data for DNS-V.* C<sub>20</sub>H<sub>12</sub>Se,  $M = 331.27$ , a pale yellow platelet,  $0.751 \times 0.075 \times 0.010$  mm, monoclinic,  $P2_1/n$ ,  $a = 12.0403(9)$ ,  $b = 4.0618(3)$ ,  $c = 27.735(2)$ , Å,  $\beta = 94.164(7)^\circ$ ,  $V = 1352.78(18)$  Å<sup>3</sup>,  $Z = 4$ ,  $\rho_{\text{calcd}} = 1.626$  g cm<sup>-3</sup>,  $T = 296$  K,  $2\theta_{\text{max}} = 50.7^\circ$ , Mo K $\alpha$  radiation,  $\lambda = 0.71075$  Å,  $\mu = 2.764$  mm<sup>-1</sup>, 8723 reflections measured, 2458 unique reflections,  $R_{\text{int}} = 3.55\%$ , 190 parameters,  $R_1 = 0.0327$  ( $I > 2\sigma(I)$ ),  $wR_2 = 0.0921$  (all data), CCDC-2003835.

*Crystal Data for C<sub>10</sub>-DNS-VW-colorless.* C<sub>40</sub>H<sub>32</sub>Se,  $M = 611.82$ , a colorless needle,  $1.000 \times 0.200 \times 0.050$  mm, monoclinic,  $C2/c$ ,  $a = 4.7733(3)$ ,  $b = 14.9798(8)$ ,  $c = 46.865(2)$  Å,  $V = 3349.4(3)$  Å<sup>3</sup>,  $Z = 4$ ,  $\rho_{\text{calcd}} = 1.213$  g cm<sup>-3</sup>,  $T = 296$  K,  $2\theta_{\text{max}} = 136.5^\circ$ , CuK $\alpha$  radiation,  $\lambda = 1.54187$  Å,  $\mu = 1.686$  mm<sup>-1</sup>, 13993 reflections measured, 3056 unique reflections,  $R_{\text{int}} = 5.11\%$ , 186 parameters,  $R_1 = 0.0350$  ( $I > 2\sigma(I)$ ),  $wR_2 = 0.1010$  (all data), CCDC-2003836.

*Crystal Data for C<sub>10</sub>-DNS-VW-yellow.* C<sub>40</sub>H<sub>32</sub>Se,  $M = 611.82$ , a yellow platelet,  $0.200 \times 0.100 \times 0.020$  mm, orthorhombic,  $Pnma$ ,  $a = 6.2320(5)$ ,  $b = 70.148(6)$ ,  $c = 7.7336(6)$  Å,  $V = 3380.8(5)$  Å<sup>3</sup>,  $Z = 4$ ,  $\rho_{\text{calcd}} = 1.202$  g cm<sup>-3</sup>,  $T = 296$  K,  $2\theta_{\text{max}} = 63.2^\circ$ , synchrotron radiation,  $\lambda = 0.8026$  Å,  $\mu = 1.528$  mm<sup>-1</sup>, 23278 reflections measured, 3730 unique reflections,  $R_{\text{int}} = 8.34\%$ , 188 parameters,  $R_1 = 0.0818$  ( $I > 2\sigma(I)$ ),  $wR_2 = 0.2899$  (all data), CCDC-2003837.

**4.3. Powder X-ray Data.** Powder X-ray diffraction patterns of C<sub>10</sub>-DNS-VW were recorded in transmission mode on a diffractometer equipped with an imaging plate detector and a nitrogen-flow high-temperature device at the RIKEN Materials Science Beamline (BL44B2) at SPring-8. Measurement conditions were as follows: capillary diameter: 0.3 mm; synchrotron radiation  $\lambda = 1.08$  Å;  $2\theta$  range:  $1.0$ – $77.58^\circ$ ; step width:  $0.01^\circ$ .

**4.4. Molecular Dynamics (MD) Simulations.** All-atom MD simulations were performed using GROMACS 4.6.7 package. The force field parameters set for calculating the intra- and interatomic interactions were generalized Amber force field<sup>43</sup> for C<sub>10</sub>-DNS-VW and phenethyl moiety and the parameters used in the previous studies,<sup>44,45</sup> for SiO<sub>2</sub> substrate, respectively. The partial atomic charges of C<sub>10</sub>-DNS-VW and the phenethyl group were obtained by restrained electrostatic potential (RESP) methodology, based on quantum chemical calculations by GAUSSIAN09 program<sup>46</sup> with 6-31G(d) basis sets, respectively. As the initial simulation, the pre-equilibration and equilibration runs for the bulk crystal structure were carried out. The number of molecules was 640 for the bulk system of both C<sub>10</sub>-DNS-VW-colorless and -yellow. The initial structure for each system was constructed from the single-crystal structure obtained in the XRD experiments. The pre-equilibration runs at 250 and 300 K were sequentially performed for 2 ns after the minimization of the steepest descent energy. During the pre-equilibration runs, the Berendsen thermostat and barostat<sup>47</sup> were used to maintain the temperature and pressure of the system, with relaxation times of 0.2 and 2.0 ps, respectively. The 10 ns equilibration runs at 300 K were performed using the Nosé–Hoover thermostat<sup>48–50</sup> and Parrinello–Rahman barostat<sup>51</sup> with relaxation times of 1.0 and 5.0 ps, respectively. The pressure was kept at 1.0 bar for each system of the bulk crystal. The initial structure of the thin films on the substrate was constructed by putting the bulk crystal structure obtained from the MD runs mentioned above onto the  $\beta$ -PTS-treated SiO<sub>2</sub>. Each of 226 phenylethyl moieties was closely positioned on a Si atom of hydroxylated SiO<sub>2</sub>. The structure of SiO<sub>2</sub> substrate was generated based on the previous study.<sup>52,53</sup> The numbers of SiO<sub>2</sub>, SiO<sub>2</sub>(OH), and SiO(OH) units contained in the substrate are 1546, 104, and 330, respectively, and its thickness was 1.493 nm. The simulated slab was located in the center, the initial size of the MD cell was  $(x, y, z) = (7.467$  nm,  $7.467$  nm,  $25.00$  nm), and enough vacuum space was left so that the intermolecular interactions with the periodic image cell along the  $z$ -direction did not occur. After the steepest descent energy minimization, the equilibration runs were carried out at 300 K using the velocity rescaling thermostat<sup>54</sup> with a relaxation time of 0.2 ps. During the equilibration run, the hydroxylated SiO<sub>2</sub> substrate was fixed because it is known to be fairly stable at room temperature and preliminary simulations showed that this treatment does not affect the layers on the substrate. Therefore, the size of the MD cell was kept constant without the pressure coupling method. To realize SAM on the SiO<sub>2</sub> substrate, harmonic positional restraints were applied to the end carbon atoms of the phenylethyl moieties. The time step was set to 2 fs because all bonds connected to hydrogen atoms were constrained with the LINCS<sup>55</sup> algorithm. The smooth particle-mesh Ewald (PME)<sup>56</sup> method was employed to treat the long-range electrostatic interactions. The real space cutoff and the grid spacing are 1.2 and 0.30 nm, respectively. The van der Waals interactions were calculated with the cutoff of 1.2 nm.

## ■ ASSOCIATED CONTENT

### Supporting Information

The Supporting Information is available free of charge at <https://pubs.acs.org/doi/10.1021/jacs.0c05522>.

Thermal analyses, thermogravimetric analyses (TGA), ionization potentials, single-crystal analyses, differential scanning calorimetric analyses, powder X-ray analyses, time-dependent absorption spectra in solution and deposited thin film, theoretical calculations, OFET device fabrication and evaluation procedure, and X-ray-diffraction measurements for solution-crystallized thin film (PDF)

Crystallographic data for DNS-V (CIF)

Crystallographic data for C<sub>10</sub>-DNS-VW-colorless (CIF)

Crystallographic data for C<sub>10</sub>-DNS-VW-yellow (CIF)

## ■ AUTHOR INFORMATION

### Corresponding Author

**Toshihiro Okamoto** – Material Innovation Research Center (MIRC) and Department of Advanced Materials Science, School of Frontier Sciences, The University of Tokyo, Kashiwa, Chiba 277-8561, Japan; National Institute of Advanced Industrial Science and Technology (AIST)-University of Tokyo Advanced Operando-Measurement Technology Open Innovation Laboratory (OPERANDO-OIL), AIST, Kashiwa, Chiba 277-8561, Japan; PRESTO, JST, Kawaguchi, Saitama 332-0012, Japan; [orcid.org/0000-0002-4783-0621](https://orcid.org/0000-0002-4783-0621);  
Email: [tokamoto@k.u-tokyo.ac.jp](mailto:tokamoto@k.u-tokyo.ac.jp)

### Authors

**Masato Mitani** – Material Innovation Research Center (MIRC) and Department of Advanced Materials Science, School of Frontier Sciences, The University of Tokyo, Kashiwa, Chiba 277-8561, Japan; [orcid.org/0000-0003-1860-2889](https://orcid.org/0000-0003-1860-2889)

**Craig P. Yu** – Material Innovation Research Center (MIRC) and Department of Advanced Materials Science, School of Frontier Sciences, The University of Tokyo, Kashiwa, Chiba 277-8561, Japan; [orcid.org/0000-0002-1423-5244](https://orcid.org/0000-0002-1423-5244)

**Chikahiko Mitsui** – Material Innovation Research Center (MIRC) and Department of Advanced Materials Science, School of Frontier Sciences, The University of Tokyo, Kashiwa, Chiba 277-8561, Japan

**Masakazu Yamagishi** – National Institute of Technology, Toyama College, Toyama, Toyama 939-8630, Japan; [orcid.org/0000-0001-6581-4812](https://orcid.org/0000-0001-6581-4812)

**Hiroyuki Ishii** – Department of Applied Physics, Faculty of Pure and Applied Sciences, University of Tsukuba, Tsukuba, Ibaraki 305-8573, Japan; [orcid.org/0000-0003-0644-1424](https://orcid.org/0000-0003-0644-1424)

**Go Watanabe** – Department of Physics, School of Science, Kitasato University, Sagami-hara, Kanagawa 252-0373, Japan; [orcid.org/0000-0001-6713-1249](https://orcid.org/0000-0001-6713-1249)

**Shohei Kumagai** – Material Innovation Research Center (MIRC) and Department of Advanced Materials Science, School of Frontier Sciences, The University of Tokyo, Kashiwa, Chiba 277-8561, Japan; [orcid.org/0000-0002-1554-054X](https://orcid.org/0000-0002-1554-054X)

**Daisuke Hashizume** – RIKEN Center for Emergent Matter Science (CEMS), Wako, Saitama 351-0198, Japan; [orcid.org/0000-0001-7152-4408](https://orcid.org/0000-0001-7152-4408)

**Shota Tanaka** – Chemistry, Materials and Bioengineering Major, Graduate School of Science and Engineering, Kansai University, Suita, Osaka 564-8680, Japan

**Masafumi Yano** – Chemistry, Materials and Bioengineering Major, Graduate School of Science and Engineering, Kansai University, Suita, Osaka 564-8680, Japan; [orcid.org/0000-0002-3268-9215](https://orcid.org/0000-0002-3268-9215)

**Tomokatsu Kushida** – Material Innovation Research Center (MIRC) and Department of Advanced Materials Science, School of Frontier Sciences, The University of Tokyo, Kashiwa, Chiba 277-8561, Japan

**Hiroyasu Sato** – Rigaku Corp., Akishima, Tokyo 196-8666, Japan

**Kunihisa Sugimoto** – Diffraction & Scattering Division, Japan Synchrotron Radiation Research Institute, Sayo-gun, Hyogo 679-5198, Japan; Institute for Integrated Cell-Material Sciences (iCeMS), Kyoto University, Kyoto 606-8501, Japan; [orcid.org/0000-0002-0103-8153](https://orcid.org/0000-0002-0103-8153)

**Takashi Kato** – Department of Chemistry and Biotechnology, School of Engineering, The University of Tokyo, Bunkyo-ku, Tokyo 113-8656, Japan; [orcid.org/0000-0002-0571-0883](https://orcid.org/0000-0002-0571-0883)

**Jun Takeya** – Material Innovation Research Center (MIRC) and Department of Advanced Materials Science, School of Frontier Sciences, The University of Tokyo, Kashiwa, Chiba 277-8561, Japan; National Institute of Advanced Industrial Science and Technology (AIST)-University of Tokyo Advanced Operando-Measurement Technology Open Innovation Laboratory (OPERANDO-OIL), AIST, Kashiwa, Chiba 277-8561, Japan; International Center for Materials Nanoarchitectonics (MANA), National Institute for Materials Science (NIMS), Tsukuba 205-0044, Japan; [orcid.org/0000-0002-7003-1350](https://orcid.org/0000-0002-7003-1350)

Complete contact information is available at: <https://pubs.acs.org/doi/10.1021/jacs.0c05522>

### Notes

The authors declare no competing financial interest.

## ■ ACKNOWLEDGMENTS

This work was supported by the JST-PRESTO programs “Molecular Technology and Creation of New Functions” (grant JPMJPR13K5 and JPMJPR12K2) and “Scientific Innovation for Energy Harvesting Technology” (JPMJPR17R2) and KAKENHI. T.O. and H.I. thank JSPS for a Grant-in-Aid for Scientific Research B (KAKENHI grant number JP17H03104 and JP18H01856). Ta.K. and G.W. thanks JSPS for Grant-in-Aid for Scientific Research on Innovative Areas (KAKENHI grant number JP19H05715 and JP19H05718). The X-ray powder diffraction experiments were performed at BL44B2 of SPring-8 (Proposal 20160029). The synchrotron single-crystal X-ray structural analysis was performed at BL02B1 of SPring-8 (Proposal 2017B1049). We gratefully thank Prof. Reiji Kumai (High Energy Accelerator Research Organization) for the measurements of in-plane and out-of-plane XRD measurements of solution-crystallized thin films. The synchrotron X-ray experiment was performed with the approval of the Photon Factory Program Advisory Committee (grant no. 2017S2-001).

## ■ REFERENCES

- (1) Bao, Z.; Locklin, J. *Organic Field-Effect Transistors*, 1st ed.; CRC Press: Boca Raton, FL, 2007.
- (2) Ebata, H.; Izawa, T.; Miyazaki, E.; Takimiya, K.; Ikeda, M.; Kuwabara, H.; Yui, T. Highly Soluble [1]Benzothieno[3,2-*b*]benzothiophene (BTBT) Derivatives for High-Performance, Solu-

tion-Processed Organic Field-Effect Transistors. *J. Am. Chem. Soc.* **2007**, *129*, 15732–15733.

(3) Yamamoto, T.; Takimiya, K. Facile Synthesis of Highly  $\pi$ -Extended Heteroarenes, Dinaphtho[2,3-*b*:2',3'-*f*]chalcogenopheno[3,2-*b*]chalcogenophenes, and Their Application to Field-Effect Transistors. *J. Am. Chem. Soc.* **2007**, *129*, 2224–2225.

(4) Kang, M. J.; Doi, I.; Mori, H.; Miyazaki, E.; Takimiya, K.; Ikeda, M.; Kuwabara, H. Alkylated Dinaphtho[2,3-*b*:2',3'-*f*]Thieno[3,2-*b*]Thiophenes (Cn-DNTTs): Organic Semiconductors for High-Performance Thin-Film Transistors. *Adv. Mater.* **2011**, *23*, 1222–1225.

(5) Nakayama, K.; Hirose, Y.; Soeda, J.; Yoshizumi, M.; Uemura, T.; Uno, M.; Li, W.; Kang, M. J.; Yamagishi, M.; Okada, Y.; Miyazaki, E.; Nakazawa, Y.; Nakao, A.; Takimiya, K.; Takeya, J. Patternable Solution-Crystallized Organic Transistors with High Charge Carrier Mobility. *Adv. Mater.* **2011**, *23*, 1626–1629.

(6) Okamoto, T.; Mitsui, C.; Yamagishi, M.; Nakahara, K.; Soeda, J.; Hirose, Y.; Miwa, K.; Sato, H.; Yamano, A.; Matsushita, T.; Uemura, T.; Takeya, J. V-Shaped Organic Semiconductors with Solution Processability, High Mobility, and High Thermal Durability. *Adv. Mater.* **2013**, *25*, 6392–6397.

(7) Mitsui, C.; Okamoto, T.; Yamagishi, M.; Tsurumi, J.; Yoshimoto, K.; Nakahara, K.; Soeda, J.; Hirose, Y.; Sato, H.; Yamano, A.; Uemura, T.; Takeya, J. High-Performance Solution-Processable N-Shaped Organic Semiconducting Materials with Stabilized Crystal Phase. *Adv. Mater.* **2014**, *26*, 4546–4551.

(8) Iino, H.; Usui, T.; Hanna, J. Liquid Crystals for Organic Thin-Film Transistors. *Nat. Commun.* **2015**, *6*, 6828.

(9) Vegiraju, S.; Chang, B.-C.; Priyanka, P.; Huang, D.-Y.; Wu, K.-Y.; Li, L.-H.; Chang, W.-C.; Lai, Y.-Y.; Hong, S.-H.; Yu, B.-C.; Wang, C.-L.; Chang, W.-J.; Liu, C.-L.; Chen, M.-C.; Facchetti, A. Intramolecular Locked Dithioalkylbithiophene-Based Semiconductors for High-Performance Organic Field-Effect Transistors. *Adv. Mater.* **2017**, *29*, 1702414.

(10) Vegiraju, S.; Luo, X.-L.; Li, L.-H.; Afraj, S. N.; Lee, C.; Zheng, D.; Hsieh, H.-C.; Lin, C.-C.; Hong, S.-H.; Tsai, H.-C.; Lee, G.-H.; Tung, S.-H.; Liu, C.-L.; Chen, M.-C.; Facchetti, A. Solution Processable Pseudo n-Thienoacenes via Intramolecular S...S Lock for High Performance Organic Field Effect Transistors. *Chem. Mater.* **2020**, *32*, 1422–1429.

(11) Vladimirov, I.; Kellermeier, M.; Geßner, T.; Molla, Z.; Grigorian, S.; Pietsch, U.; Schaffroth, L. S.; Kühn, M.; May, F.; Weitz, R. T. High-Mobility, Ultrathin Organic Semiconducting Films Realized by Surface-Mediated Crystallization. *Nano Lett.* **2018**, *18*, 9–14.

(12) Usta, H.; Kim, D.; Ozdemir, R.; Zorlu, Y.; Kim, S.; Ruiz Delgado, M. C.; Harbuzaru, A.; Kim, S.; Demirel, G.; Hong, J.; Ha, Y.-G.; Cho, K.; Facchetti, A.; Kim, M.-G. High Electron Mobility in [1]Benzothieno[3,2-*b*] [1]benzothiophene-Based Field-Effect Transistors: Toward n-Type BTBTs. *Chem. Mater.* **2019**, *31*, S254–S263.

(13) Okamoto, T.; Kumagai, S.; Fukuzaki, E.; Ishii, H.; Watanabe, G.; Niitsu, N.; Annaka, T.; Yamagishi, M.; Tani, Y.; Sugiura, H.; Watanabe, T.; Watanabe, S.; Takeya, J. Robust, high-performance n-type organic semiconductors. *Sci. Adv.* **2020**, *6*, eaaz0632.

(14) Nakahara, K.; Mitsui, C.; Okamoto, T.; Yamagishi, M.; Matsui, H.; Ueno, T.; Tanaka, Y.; Yano, M.; Matsushita, T.; Soeda, J.; Hirose, Y.; Sato, H.; Yamano, A.; Takeya, J. Furan Fused V-Shaped Organic Semiconducting Materials with High Emission and High Mobility. *Chem. Commun.* **2014**, *50*, S342–S344.

(15) Mitsui, C.; Kubo, W.; Tanaka, Y.; Yamagishi, M.; Annaka, T.; Dosei, H.; Yano, M.; Nakamura, K.-i.; Iwasawa, D.; Hasegawa, M.; Takehara, T.; Suzuki, T.; Sato, H.; Yamano, A.; Takeya, J.; Okamoto, T. Impact of Phenyl Groups on Oxygen-Bridged V-Shaped Organic Semiconductors. *Chem. Lett.* **2017**, *46*, 338–341.

(16) Mitsui, C.; Tsuyama, H.; Shikata, R.; Murata, Y.; Kuniyasu, H.; Yamagishi, M.; Ishii, H.; Yamamoto, A.; Hirose, Y.; Yano, M.; Takehara, T.; Suzuki, T.; Sato, H.; Yamano, A.; Fukuzaki, E.; Watanabe, T.; Usami, Y.; Takeya, J.; Okamoto, T. High Performance Solution-Crystallized Thin-Film Transistors Based on V-Shaped

Thieno[3,2-*f*:4,5-*f'*]bis[1]benzothiophene Semiconductors. *J. Mater. Chem. C* **2017**, *5*, 1903–1909.

(17) Mitsui, C.; Yamagishi, M.; Shikata, R.; Ishii, H.; Matsushita, T.; Nakahara, K.; Yano, M.; Sato, H.; Yamano, A.; Takeya, J.; Okamoto, T. Oxygen- and Sulfur-Bridged Bianthracene V-Shaped Organic Semiconductors. *Bull. Chem. Soc. Jpn.* **2017**, *90*, 931–938.

(18) Okamoto, T.; Yu, C. P.; Mitsui, C.; Yamagishi, M.; Ishii, H.; Takeya, J. Bent-Shaped p-Type Small-Molecule Organic Semiconductors: A Molecular Design Strategy for Next-Generation Practical Applications. *J. Am. Chem. Soc.* **2020**, *142*, 9083–9096.

(19) Maliakal, A.; Raghavachari, K.; Katz, H.; Chandross, E.; Siegrist, T. Photochemical Stability of Pentacene and a Substituted Pentacene in Solution and in Thin Films. *Chem. Mater.* **2004**, *16*, 4980–4986.

(20) Solubility Parameter. *Bulletin of the American Group. International Institute for Conservation of Historic and Artistic Works* **1968**, *8*, 20–24

(21) Mitsui, C.; Annaka, T.; Nakamura, K.-i.; Mitani, M.; Hashizume, D.; Nakahara, K.; Yamagishi, M.; Ueno, T.; Tanaka, Y.; Yano, M.; Iwasawa, D.; Hasegawa, M.; Sato, H.; Yamano, A.; Takeya, J.; Okamoto, T. Alkylated Oxygen-Bridged V-Shaped Molecules: Impacts of the Substitution Position and Length of the Alkyl Chains on the Crystal Structures and Fundamental Properties in Aggregated Forms. *Polym. J.* **2017**, *49*, 215–221.

(22) Okamoto, T.; Kudoh, K.; Wakamiya, A.; Yamaguchi, S. General Synthesis of Thiophene and Selenophene-Based Heteroacenes. *Org. Lett.* **2005**, *7*, 5301–5304.

(23) Takimiya, K.; Kunugi, Y.; Konda, Y.; Ebata, H.; Toyoshima, Y.; Otsubo, T. 2,7-Diphenyl[1]benzoselenopheno[3,2-*b*] [1]benzoselenophene as a Stable Organic Semiconductor for a High-Performance Field-Effect Transistor. *J. Am. Chem. Soc.* **2006**, *128*, 3044–3050.

(24) Osuna, R. M.; Ortiz, R. P.; Okamoto, T.; Suzuki, Y.; Yamaguchi, S.; Hernández, V.; López Navarrete, J. T. Thiophene- and Selenophene-Based Heteroacenes: Combined Quantum Chemical DFT and Spectroscopic Raman and UV–Vis–NIR Study. *J. Phys. Chem. B* **2007**, *111*, 7488–7496.

(25) Yamada, K.; Okamoto, T.; Kudoh, K.; Wakamiya, A.; Yamaguchi, S.; Takeya, J. Single-Crystal Field-Effect Transistors of Benzannulated Fused Oligothiophenes and Oligoselenophenes. *Appl. Phys. Lett.* **2007**, *90*, No. 072102.

(26) Izawa, T.; Miyazaki, E.; Takimiya, K. Solution-Processible Organic Semiconductors Based on Selenophene-Containing Heteroarenes, 2,7-Dialkyl[1]benzoselenopheno[3,2-*b*] [1]benzoselenophenes (Cn-BSBSs): Syntheses, Properties, Molecular Arrangements, and Field-Effect Transistor Characteristics. *Chem. Mater.* **2009**, *21*, 903–912.

(27) Oyama, T.; Yang, Y. S.; Matsuo, K.; Yasuda, T. Effects of Chalcogen Atom Substitution on the Optoelectronic and Charge-Transport Properties in Picene-Type  $\pi$ -Systems. *Chem. Commun.* **2017**, *53*, 3814–3817.

(28) Sugino, H.; Takimiya, K. Effects of Selenium Atoms on [1]Benzochalcogenopheno[3,2-*b*] [1]benzochalcogenophene-Based Organic Semiconductors. *Chem. Lett.* **2017**, *46*, 345–347.

(29) Wang, C.; Abbas, M.; Wantz, G.; Kawabata, K.; Takimiya, K. “Heavy-Atom Effects” in the Parent [1]Benzochalcogenopheno[3,2-*b*] [1]benzochalcogenophene System. *J. Mater. Chem. C* **2020** DOI: 10.1039/D0TC01408G.

(30) Kondo, Y.; Shilai, M.; Uchiyama, M.; Sakamoto, T. TMP–Zincate as Highly Chemoselective Base for Directed Ortho Metalation. *J. Am. Chem. Soc.* **1999**, *121*, 3539–3540.

(31) Uchiyama, M.; Miyoshi, T.; Kajihara, Y.; Sakamoto, T.; Otani, Y.; Ohwada, T.; Kondo, Y. Generation of Functionalized Asymmetric Benzynes with TMP–Zincates. Effects of Ligands on Selectivity and Reactivity of Zincates. *J. Am. Chem. Soc.* **2002**, *124*, 8514–8515.

(32) Uchiyama, M.; Kobayashi, Y.; Furuyama, T.; Nakamura, S.; Kajihara, Y.; Miyoshi, T.; Sakamoto, T.; Kondo, Y.; Morokuma, K. Generation and Suppression of 3-/4-Functionalized Benzynes Using Zinc Ate Base (TMP–Zn–ate): New Approaches to Multisubstituted Benzenes. *J. Am. Chem. Soc.* **2008**, *130*, 472–480.

- (33) Maaninen, A.; Chivers, T.; Parvez, M.; Pietikäinen, J.; Laitinen, R. S. Syntheses of THF Solutions of  $\text{SeX}_2$  ( $X = \text{Cl}, \text{Br}$ ) and a New Route to Selenium Sulfides  $\text{SenS8-n}$  ( $n = 1-5$ ): X-ray Crystal Structures of  $\text{SeCl}_2(\text{tht})_2$  and  $\text{SeCl}_2\cdot\text{tmtu}$ . *Inorg. Chem.* **1999**, *38*, 4093–4097.
- (34) Chelucci, G.; Figus, S.  $\text{NaBH}_4$ -TMEDA and a Palladium Catalyst as Efficient Regio- and Chemoselective System for the Hydrodehalogenation of Halogenated Heterocycles. *J. Mol. Catal. A: Chem.* **2014**, *393*, 191–209.
- (35) Meng, H.; Bao, Z.; Lovinger, A. J.; Wang, B.-C.; Mujsce, A. M. High Field-Effect Mobility Oligofluorene Derivatives with High Environmental Stability. *J. Am. Chem. Soc.* **2001**, *123*, 9214–9215.
- (36) Curtis, M. D.; Cao, J.; Kampf, J. W. Solid-State Packing of Conjugated Oligomers: From  $\pi$ -Stacks to the Herringbone Structure. *J. Am. Chem. Soc.* **2004**, *126*, 4318–4328.
- (37) Kato, K.; Tanaka, H. Visualizing Charge Densities and Electrostatic Potentials in Materials by Synchrotron X-Ray Powder Diffraction. *Adv. Phys. X* **2016**, *1*, 55–80.
- (38) Sagara, Y.; Yamane, S.; Mitani, M.; Weder, C.; Kato, T. Mechanoresponsive Luminescent Molecular Assemblies: An Emerging Class of Materials. *Adv. Mater.* **2016**, *28*, 1073–1095.
- (39) Valeev, E. F.; Coropceanu, V.; da Silva Filho, D. A.; Salman, S.; Brédas, J.-L. Effect of Electronic Polarization on Charge-Transport Parameters in Molecular Organic Semiconductors. *J. Am. Chem. Soc.* **2006**, *128*, 9882–9886.
- (40) Kuroda, Y.; Ishii, H.; Yoshino, S.; Kobayashi, N. Second Highest Occupied Molecular Orbital Effects on the Valence Band Structure of Organic Semiconductors. *Jpn. J. Appl. Phys.* **2019**, *58*, S11B27.
- (41) Uemura, T.; Hirose, Y.; Uno, M.; Takimiya, K.; Takeya, J. Very High Mobility in Solution-Processed Organic Thin-Film Transistors of Highly Ordered [1]Benzothieno[3,2-*b*]benzothiophene Derivatives. *Appl. Phys. Express* **2009**, *2*, 111501.
- (42) To determine the cause of this behavior and to solve the problem, a study of the annealing condition for the device is underway in our laboratory.
- (43) Wang, J.; Wolf, R. M.; Caldwell, J. W.; Kollman, P. A.; Case, D. A. Development and Testing of a General Amber Force Field. *J. Comput. Chem.* **2004**, *25*, 1157–1174.
- (44) Cygan, R. T.; Liang, J.-J.; Kalinichev, A. G. Molecular Models of Hydroxide, Oxyhydroxide, and Clay Phases and the Development of a General Force Field. *J. Phys. Chem. B* **2004**, *108*, 1255–1266.
- (45) Emami, F. S.; Puddu, V.; Berry, R. J.; Varshney, V.; Patwardhan, S. V.; Perry, C. C.; Heinz, H. Force Field and a Surface Model Database for Silica to Simulate Interfacial Properties in Atomic Resolution. *Chem. Mater.* **2014**, *26*, 2647–2658.
- (46) Frisch, M. J.; Trucks, G. W.; Schlegel, H. B.; Scuseria, G. E.; Robb, M. A.; Cheeseman, J. R.; Scalmani, G.; Barone, V.; Mennucci, B.; Petersson, G. A.; Nakatsuji, H.; Caricato, M.; Li, X.; Hratchian, H. P.; Izmaylov, A. F.; Bloino, J.; Zheng, G.; Sonnenberg, J. L.; Hada, M.; Ehara, M.; Toyota, K.; Fukuda, R.; Hasegawa, J.; Ishida, M.; Nakajima, T.; Honda, Y.; Kitao, O.; Nakai, H.; Vreven, T.; Montgomery, J. A.; Peralta, J. J. E.; Ogliaro, F.; Bearpark, M.; Heyd, J. J.; Brothers, E.; Kudin, K. N.; Staroverov, V. N.; Keith, T.; Kobayashi, R.; Normand, J.; Raghavachari, K.; Rendell, A.; Burant, J. C.; Iyengar, S. S.; Tomasi, J.; Cossi, M.; Rega, N.; Millam, J. M.; Klene, M.; Knox, J. E.; Cross, J. B.; Bakken, V.; Adamo, C.; Jaramillo, J.; Gomperts, R.; Stratmann, R. E.; Yazyev, O.; Austin, A. J.; Cammi, R.; Pomelli, C.; Ochterski, J. W.; Martin, R. L.; Morokuma, K.; Zakrzewski, V. G.; Voth, G. A.; Salvador, P.; Dannenberg, J. J.; Dapprich, S.; Daniels, A. D.; Farkas, O.; Foresman, J. B.; Ortiz, J. V.; Cioslowski, J.; Fox, D. J. *Gaussian 09, Revision D. 01*; Gaussian, Inc., Wallingford, CT, 2013.
- (47) Berendsen, H. J. C.; Postma, J. P. M.; van Gunsteren, W. F.; DiNola, A.; Haak, J. R. Molecular Dynamics with Coupling to an External Bath. *J. Chem. Phys.* **1984**, *81*, 3684–3690.
- (48) Nosé, S. A Unified Formulation of the Constant Temperature Molecular Dynamics Methods. *J. Chem. Phys.* **1984**, *81*, 511–519.
- (49) Nosé, S. A Molecular Dynamics Method for Simulations in the Canonical Ensemble. *Mol. Phys.* **1984**, *52*, 255–268.
- (50) Hoover, W. G. Canonical Dynamics: Equilibrium Phase-Space Distributions. *Phys. Rev. A: At., Mol., Opt. Phys.* **1985**, *31*, 1695–1697.
- (51) Parrinello, M.; Rahman, A. Polymorphic Transitions in Single Crystals: A New Molecular Dynamics Method. *J. Appl. Phys.* **1981**, *52*, 7182–7190.
- (52) Kroutil, O.; Chval, Z.; Skelton, A. A.; Předota, M. Computer Simulations of Quartz (101)–Water Interface over a Range of pH Values. *J. Phys. Chem. C* **2015**, *119*, 9274–9286.
- (53) Wei, T.; Sajib, M. S. J.; Samieegohar, M.; Ma, H.; Shing, K. Self-Assembled Monolayers of an Azobenzene Derivative on Silica and Their Interactions with Lysozyme. *Langmuir* **2015**, *31*, 13543–13552.
- (54) Bussi, G.; Donadio, D.; Parrinello, M. Canonical Sampling through Velocity Rescaling. *J. Chem. Phys.* **2007**, *126*, No. 014101.
- (55) Hess, B.; Bekker, H.; Berendsen, H. J. C.; Fraaije, J. G. E. M. LINCS: A Linear Constraint Solver for Molecular Simulations. *J. Comput. Chem.* **1997**, *18*, 1463–1472.
- (56) Darden, T.; York, D.; Pedersen, L. Particle Mesh Ewald: An  $N \log(N)$  Method for Ewald Sums in Large Systems. *J. Chem. Phys.* **1993**, *98*, 10089–10092.